Transformation of the phyllomanganate vernadite to tectomanganates with small tunnel sizes: Favorable geochemical conditions and fate of associated Co

Zhongkuan Wu, Bruno Lanson, Xionghan Feng, Hui Yin, Wenfeng Tan, Feng He, Fan Liu

Transformation of the phyllomanganate vernadite to tectomanganates with small tunnel sizes: Favorable geochemical conditions and fate of associated Co

Zhongkuan Wu[a,b,c], Bruno Lanson[*,c], Xionghan Feng[b], Hui Yin[b], Wenfeng Tan[b], Feng He[a], Fan Liu[*,b]

[a]*College of Environment, Zhejiang University of Technology, Hangzhou 310014, China*

[b]*Key Laboratory of Arable Land Conservation (Middle and Lower Reaches of Yangtse River) Ministry of Agriculture, College of Resources and Environment, Huazhong Agricultural University, Wuhan 430070, China*

[c]*Univ. Grenoble Alpes, Univ. Savoie Mont Blanc, CNRS, IRD, Univ. Gustave Eiffel, ISTerre, F-38000 Grenoble, France*

** Corresponding author:*

bruno.lanson@univ-grenoble-alpes.fr; *liufan@mail.hzau.edu.cn*

Keywords: Mn oxide; Phyllomanganate precursor; Birnessite; Tectomanganates; Cryptomelane; Nsutite; XRD; EXAFS; Nitric acid treatment; Cobalt, Transition metal

Dataset for this article contains: Chemical compositions; XAS data at Mn and Co K-edges; XRD data; Chemical analyses upon nitric acid treatment.

Dataset is available at: https://data.mendeley.com/datasets/27369v78sv/2

Abstract

The present work uncovers the geochemical control on the nature (tunnel size) of the tectomanganates formed from layered precursors, and thus provides insights into the formation of Mn oxides in natural environments. Large tunnel sizes are favored under circum-neutral conditions, whereas low pH conditions favor the formation of tectomanganates with smaller tunnel sizes. Both the increased proportions of Mn(III) in vernadite/birnessite layers resulting from low pH conditions and the subsequent enhancement of Mn(III) disproportionation during subsequent transformation contribute to the formation of tectomanganates with smaller tunnel sizes. The fate of foreign elements during the phyllomanganate-to-tectomanganate mineral transformation is another important aspect of this mineral transformation, together with the impact of these elements on the transformation. Layered and tunnel Mn oxides have indeed a pivotal influence on the geochemical cycling of transition metals, including Co, that possess a strong affinity for these mineral species. The present experimental work shows that the formation of todorokite (3×3 tunnel size), hollandite (2×2), or nsutite (intergrown 1×1 and 1×2 fragments) is essentially unaffected by limited Co-enrichment (≤5 at.%) of the initial phyllomanganate structure. Higher Co contents reduce the content of Jahn-Teller distorted Mn(III) octahedra in layered precursor and hamper the phyllomanaganate-to-tectomanganate transformation. Finally, Co is retained in the structure of todorokite and hollandite during their formation under circum-neutral conditions whereas part (~20%) of the Co present in layered precursors is expelled out of the framework and/or sorbed to nsutite formed under acidic conditions. This effect is induced by the reduced stability of Co(III) octahedra when the relative proportion of corner-sharing linkages increases. In turn, this effect influences Co structural incorporation in different Mn oxides and its potential release to solution.

1. INTRODUCTION

Manganese oxides are common in ferro-manganese nodules or polymetallic crusts found in aquatic and terrestrial environments (Chukhrov et al., 1981, 1987; Hein et al., 1988; Bodeï et al., 2007). Among these oxides, layered oxides (phyllomanganates: birnessite, vernadite, buserite, asbolane, and lithiophorite) and tectomanganates with medium [2×2: hollandite (Ba^{2+}) and cryptomelane (K^{+})] and large tunnels [3×3: todorokite] have attracted special attention. The sustained interest for these minerals results from their ubiquity in a variety of natural environments, their common enrichment in transition metals and rare-earth elements (Burns and Burns, 1978; Ostwald, 1984; Hein et al., 1988; Post, 1999), and from their key influence on the transport and fate of organic and inorganic contaminants (McKenzie, 1989; Post, 1999).

By contrast, tectomanganates with smaller tunnel sizes (1×1: pyrolusite; 1×2: ramsdellite; intergrowth of 1×1 and 1×2 fragments: nsutite – Zwicker et al., 1962; Post, 1999) are abundant in manganese ore deposits worldwide (Zwicker et al., 1962; Turner and Buseck, 1983; Parc et al., 1989; Nicholson, 1992 and references therein). In addition to the widespread use of manganese in metallic alloys, these economic deposits are mined for the electro-chemical performance of the tectomanganates with smaller tunnel sizes (Turner and Buseck, 1983). They usually result from intense long-term supergene weathering of terrestrial and marine deposits (see for example the review of Nicholson, 1992 and references therein), and more especially of Mn-bearing carbonates and silicates under humid tropical or subtropical climates (Mücke et al., 1999; Dekonink et al., 2019). In these contexts, tectomanganate formation is not meant to imply layered precursors, despite contradictory observations in lateritic profiles (Parc et al., 1989). Formation of tectomanganates such as nsutite from layered precursors was also reported experimentally (Tu et al., 1994; Luo et al., 2018). More generally, tectomanganate formation from phyllomanganate precursors has attracted special attention (Golden et al., 1986, 1987; Feng et al., 2004; Shen et al., 2005; Bodeï et al., 2007), owing to the major contribution of this formation pathway to the natural

abundance of tectomanganates. Mn(III) migration out of the octahedral MnO_2 layers to release steric strains arising from the Jahn-Teller distortion of Mn(III) octahedra and/or layer kinking at these structurally weak points appear as the most likely mechanisms for the formation of tectomanganates having large and medium tunnel sizes, such as todorokite (Atkins et al., 2014) and hollandite/cryptomelane (Grangeon et al., 2014, 2015).

In nodules and crusts, Mn oxide enrichment in transition metals and rare earth elements occurs through sorption, isomorphous substitution (structural incorporation), or intimate association with (oxyhydr)oxides, and resulting concentrations of these elements may reach several percents (Taylor, 1968; Burns and Burns, 1978; Manceau et al., 1987, 2007; Hein et al., 1988; Post, 1999; Marcus et al., 2004; Bodeï et al., 2007; Peacock and Sherman, 2007; Asavin et al., 2015). Together with Ni, Co is among the most common transition metals found in association with, and structurally incorporated in, both layered and tunnel Mn oxides (Taylor, 1968; Manceau et al., 1987, 1997; Hein et al., 1988; McKenzie, 1989; Kay et al., 2001; Asavin et al., 2015; Simanova and Peña, 2015; Wu et al., 2019). (Co,Ni) enrichment is for example typical for the so-called "hydrogenetic" Mn oxides (Bonatti et al., 1972; Choi and Hariya, 1992; Nicholson et al. 1992). Specifically, surface-catalyzed oxidization of Co(II) by Mn(III) and subsequent migration of Co(III) in former Mn(III) octahedral sites account for Co enrichment in phyllomanganates (Manceau et al., 1997; Simanova and Peña, 2015). Co(III)-for-Mn(III) substitutions are sterically favored and release steric strains arising from the presence of Jahn-Teller distorted Mn(III) octahedra, and thus negatively influence birnessite conversion to todorokite (Drits et al., 1997; Manceau et al., 1997; Gaillot et al., 2007; Yin et al., 2015; Wu et al., 2019). In addition, high Co concentrations (>5 at.%) in layered Mn oxides commonly leads to the formation of asbolane as described by Chukhrov et al. (1987), precluding further the transformation to tunnel structures. When this transformation occurs, that is experimentally for Co content <7.7 at.%, Co is essentially retained in the solid phase, being mainly present in

octahedral sites sharing only edges with adjacent octahedra (Mn1/Mn3 sites of todorokite – Wu et al., 2019; Wegorzewski et al., 2020). Co may also be structurally incorporated in hollandite/cryptomelane (Li et al., 2015). Although favored in tectomanganates with large and medium tunnel sizes, Co contents of 1-2 at.% [Co/(Co+Mn)] have also been reported in natural pyrolusite (e.g., Lambiv Dzemua et al., 2013).

The fate of Co during the transformation from layered precursors to tectomanganates with medium-to-small tunnel sizes remains poorly documented, however. The present work thus aimed at preparing nsutite and hollandite from the same Co-containing vernadite precursor, a phyllomanganate common in soils (Chukhrov et al., 1981; McKenzie, 1989; Vodyanitskii, 2006, 2009), sediments (Bodeï et al., 2007), and deep-sea Mn nodules (Chukhrov et al., 1987; Hein et al., 1988), using a reflux treatment mimicking natural processes (Feng et al., 2004; Atkins et al., 2014). Layered precursors and reflux products were characterized using chemical analysis, X-ray diffraction, Mn/Co K-edge X-ray absorption spectroscopy, and nitric acid treatment. Transformation processes were determined through the characterization of intermediate reaction products. In addition, special attention was paid to decipher the fate of Co during the formation of the two tectomanganates. The present work thus provides significant new insight into the geochemical conditions enhancing the formation of tectomanganates with contrasting tunnel sizes, and the crystal-chemical features driving the fate of associated foreign metal elements in natural environments.

2. MATERIALS AND METHODS

2.1. Preparation of Co-containing vernadite

Vernadite was synthesized according to a modified version of the protocol reported by Villalobos et al. (2003). Specifically, 300 mL of a 0.2 M $KMnO_4$ solution, which was boiled and cooled to room temperature, were dropped into 300 mL of a 0.667 M

NaOH solution at a 5 mL/min rate. Next, 300 mL of a solution containing 23.7 g of $MnCl_2 \cdot 4H_2O$ and 2.37 g of $CoCl_2 \cdot 6H_2O$ [Co/(Co+Mn) = 5.3 at.%] were added to the mix at a 5 mL/min rate. The resulting suspension was left to settle for 2 hrs (final pH of the supernatant was 4.32), filtered and washed with ultrapure water (18.2 MΩ.cm) until its conductivity was <20 µS/cm. Part (~110 mL) of this suspension was freeze dried, this sample being referred to as CoV.

2.2. Transformation of Co-containing vernadite to nsutite

Half of the remaining CoV suspension was sampled, and its volume adjusted to 500 mL with ultrapure water. This suspension was then equilibrated at pH 4 for 3 days using HNO_3 or NaOH. A 100 mL aliquot was sampled and washed, the resulting sample being referred to as CoV-pH4. Most of the remaining 400 mL suspension was transferred to a flask and refluxed at 100 °C for 2 days, during which 30 mL aliquots were sampled at different time intervals. After cooling to room temperature, the final pH of the supernatant was 5.52. The samples were named CoV-pH4-Re-nn, nn being the reflux time. For example, the final product is referred to as CoV-pH4-Re-2d. In addition, sample CoV-0.5M H^+-Re was obtained by refluxing an aliquot of CoV in a 0.5 M HNO_3 aqueous solution.

2.3. Transformation of Co-containing vernadite to hollandite

The other half of the remaining suspension was contacted with 500 mL of a 1 M NaCl solution for 1 day (Zhao et al., 2015), and washed until conductivity was <20 µS/cm. The resulting homoionic suspension was then resuspended in a 0.5 M $BaCl_2$ solution for 1 day and washed again with ultra-pure water until conductivity was <20 µS/cm. The volume of this suspension was adjusted to 500 mL, and its pH equilibrated to 7.50 ±0.05 for 1 day. The resulting sample is referred to as CoV-Ba. 400 mL of the CoV-Ba suspension was then refluxed at 100 °C for 2 days, leading to sample CoV-Ba-Re. After cooling to room temperature, the final pH of the supernatant was 6.12. All the

above solid samples were retrieved through centrifugation and freeze-dried.

2.4. Sample characterization

X-ray diffraction was performed on a Bruker D8 diffractometer, equipped with Cu Kα radiation (λ = 1.5418 Å) and a SolXE solid-state detector (Baltic Scientific Equipments). Data was collected from 2-90 °2θ Cu Kα in step mode with 40 s counting times per 0.04 º2θ step. Sample chemical composition was measured in duplicate using inductively-coupled plasma spectrometry (ICP-OES Varian 720ES) after dissolution of the samples in $NH_2OH.HCl$.

To assess the relative proportion of elements structurally incorporated in the solids and sorbed at their surface, 0.1 g aliquots were acid-washed in 250 mL of a 1 M HNO_3 solution under moderate stirring at room temperature (23 °C). 5 mL aliquots of this suspension were sampled at different time intervals and immediately filtered through a 0.22 µm membrane to determine the release of Mn, Co, and Ba, the contents of which were analyzed by ICP-OES.

Mn/Co K-edge Extended X-ray Absorption Fine Structure (EXAFS) spectra were collected at room temperature on the 1W1B beamline of the Beijing Synchrotron Radiation Facility (BSRF) to determine Mn/Co local environments in both layered precursors and reflux products. Data was collected in transmission (Mn K-edge) or fluorescence (Co K-edge) mode, a metallic Mn/Co foil being used as reference for energy calibration. Athena and Artemis softwares were used to process and simulate EXAFS spectra (Ravel and Newville, 2005). Path simulations for Mn K-edge EXAFS were performed over the 1-4 Å (R+ΔR) range in r-space and over 3.1–12.7 $Å^{-1}$ in k-space, with an amplitude reduction factor (S_0^2) of 0.8 (Grangeon et al., 2010). Path simulations for Co K-edge EXAFS were performed over the 1-3.8 Å (R+ΔR) range in r-space and over 3.2–10.5 $Å^{-1}$ in k-space, with an amplitude reduction factor (S_0^2) of 0.877 (Yin et al., 2014).

The Mn average oxidation state (AOS) of layered precursors and reflux products

was determined by applying a linear combination fitting method to the Mn K-edge XANES 1st derivative data, that is specifically designed for the determination of Mn valence states in mixed-valent Mn oxides (the so-called Combo method – Manceau et al., 2012). The reference compounds used for Mn(II), Mn(III) and Mn(IV) were those of the original study, the uncertainty on the relative proportion of the different Mn oxidation states being ±4% (Manceau et al., 2012).

3. RESULTS

3.1. Elemental composition

Co/(Co+Mn) ratios are about the same for all analyzed samples at 5.05-5.28 at.% (Table 1). Limited Co, or Mn, is thus removed, exchanged, or desorbed from the solid phase during pH equilibration, cation exchange, or reflux. On the other hand, all Na^+ initially present in CoV is replaced by protons following equilibration at pH 4, when only ~1/3 of K initially present is replaced. An additional ~1/5 of K is released during the reflux of CoV-pH4. For CoV-Ba, after two-steps (Na^+ and Ba^{2+}) of exchange, no K and only minor Na were detected. The significant increase in Mn content from layered precursors to their reflux products is most likely related to their contrasting H_2O contents and the related "dilution" effect. Birnessite/vernadite contains indeed ~2% adsorbed H_2O and ~7% interlayer H_2O (Lanson et al., 2002) compared to ~3.0% of adsorbed and lattice H_2O in nsutite (Said, 2020).

3.2. Mn average oxidation state

During the reflux process, the Mn AOS of Co-containing layered precursors increases systematically (Table 2). This increase is enhanced under low pH conditions as shown by the respective AOS determined for CoV-0.5M H^+-Re-2d and CoV-pH4-Re-2d (3.90 and 3.72, respectively). This increase contrasts with the Mn AOS stability reported during birnessite conversion to todorokite under similar reflux conditions

214 (Atkins et al., 2014; Wu et al., 2019).

215 **3.3. Powder XRD patterns**

216 All three layered precursors (CoV, CoV-pH4, and CoV-Ba), display a weak and
217 broad peak at ~7 Å (Fig. 1a), indicative of a limited periodicity of MnO_6 octahedral
218 layer stacking along the c* axis (Drits et al., 1997; Villalobos et al., 2006; Grangeon et
219 al., 2008; Lanson et al., 2008; Yin et al., 2012). XRD patterns obtained for these three
220 samples display also an asymmetric peak at ~2.43 Å and a broad maximum at ~1.41 Å,
221 whose position and shape are typical of octahedral layers having hexagonal symmetry.
222 Together, these three peaks are typical for vernadite (Fig. 1a – Chukhrov et al., 1987;
223 Drits et al., 2007). In addition, XRD pattern of CoV-pH4 shows weak modulations at
224 3.95, 2.14, and 1.64 Å, indicative of a minor nsutite contribution (ICDD#17-0510)
225 resulting from low-pH conditions maintained for several days (Fig. S1).

226 Compared to those of their layered precursors, XRD patterns of the reflux products
227 display additional reflections (Fig. 1b). For example, the XRD pattern of CoV-pH4-Re-
228 2d display reflections at 4.02, 2.45, 2.15, and 1.67 Å, consistent with the prominent
229 lines of manganoan nsutite (ICDD#14-0614 – Fig. S1). Nsutite consists in the
230 intergrowth of pyrolusite and ramsdellite fragments, thus displaying both 1×1 and 1×2
231 tunnel sizes (Zwicker et al., 1962; Turner and Buseck, 1983; Post, 1999), its manganoan
232 equivalent containing presumably a significant amount of Mn(II,III) (Zwicker et al.,
233 1962). XRD pattern of CoV-pH4-Re-1h is essentially similar to that of CoV-pH4-Re-
234 2d, except for a lower signal-to-noise ratio (Fig. 1b). Mineralogical transformation from
235 the vernadite precursor to manganoan nsutite thus occurs very early during the reflux
236 process, the initial crystallization stage being followed by a steady crystal growth. In
237 addition, the persistence of the ~7.0 Å reflection in XRD patterns of both CoV-pH4-
238 Re-1h and CoV-pH4-Re-2d indicates the presence of residual vernadite.

239 Although the XRD pattern of CoV-0.5M H^+-Re-2d looks like that of the former,
240 reflections of CoV-0.5M H^+-Re-2d are shifted towards higher angles, compared to those

of the latter. Peak positions in CoV-0.5M H^+-Re-2d are consistent with the presence of ideal nsutite (ICDD#17-0510), rather than manganoan nsutite, consistent with the higher Mn AOS determined in this sample, compared to CoV-pH4-Re-2d. Finally, XRD pattern of CoV-Ba-Re is similar to that of hollandite (ICDD #38-0476 – Fig. S1), a tectomanganate with a uniform 2×2 tunnel size (Post et al., 1982; Miura, 1986).

3.4. Mn local environment

Mn K-edge EXAFS spectra collected for both layered precursors and reflux products (Fig. 2a) have similar frequency, except over the 7.0-9.5 $Å^{-1}$ "indicator region" (Marcus et al., 2004). Specifically, layered precursors have troughs at ~7.5 $Å^{-1}$ while their reflux products display weak peaks at the same frequency. On the contrary, layered precursors display sharp peaks of similar intensities at ~8.2 $Å^{-1}$, whereas reflux products display much weaker peaks at this frequency, that of CoV-0.5M H^+-Re-2d almost vanishing. Mn K-edge spectra of the three layered precursors are essentially similar over the 8.5-9.2 $Å^{-1}$ range, whereas spectra of CoV-0.5M H^+-Re-2d and CoV-Ba-Re display distinct peaks at ~8.6 $Å^{-1}$ and ~8.9 $Å^{-1}$, respectively (Fig. 2a). The contrasting profiles of Mn K-edge spectra over this "indicator region" are indicative of different contents and distributions of Mn(III) and Mn(IV) in layered precursors, and of variable tunnel sizes in reflux products (McKeown and Post, 2001; Bargar et al., 2005; Webb et al., 2005; Toner et al., 2006; Bodeï et al., 2007).

The Fourier transforms (FTs) of these EXAFS spectra (Fig. 2b) display three main peaks at ~1.5, ~2.5, and ~3.0 Å (R+ΔR) that correspond to the nearest Mn-O, edge-sharing Mn-Me (Me = Mn, Co), and corner-sharing Mn-Me shells, respectively (McKeown and Post, 2001; Webb et al., 2005). Positions of these three peaks are similar for all samples but the relative intensities of the latter two peaks vary between layered precursors and reflux products (Fig. 2b). The intensity at ~2.5 Å (R+ΔR) decreases indeed from layered precursors to reflux products whereas an opposite trend is visible at ~3.0 Å (R+ΔR). Both trends are maximized for CoV-0.5M H^+-Re-2d, that displays

lowest intensity at ~2.5 Å (R+ΔR) and highest at ~3.0 Å (R+ΔR), indicative of low numbers of edge-sharing linkages (ESL) and of high numbers of corner-sharing linkages (CSL). Peaks at ~5.2 Å (R+ΔR) represent the second-neighbor Mn-Me in octahedral sheets (Bargar et al., 2005; Webb et al., 2005; Toner et al., 2006; Wu et al., 2019). Consistent with the trend observed for the first edge-sharing Mn-Me shell, this peak decreases in intensity from layered precursors to reflux products, indicative of the decreasing proportion and/or size of layered fragments.

Coordination numbers (CN) and distances typical for the different shells are derived from the simulation of Mn K-edge EXAFS spectra and of their FTs in both k and r spaces (Table S1 – Grangeon et al., 2010). In layered precursors, Mn atom have ~4 nearest Mn neighbors, a number much lower than the theoretical value of 6 even taking experimental uncertainties into account. Small particle size, and related edge effect (Bargar et al., 2005), and presence of vacant octahedral sites likely account for the observed reduction of CN (Grangeon et al., 2010). On the other hand, CN of Mn-Me CSL increases from layered precursors to their reflux products leading to a remarkable increase in the CN_C/CN_E ratio, consistent with a phyllomanganate-to-tectomanganate conversion (Kim et al., 2003; Webb et al., 2005; Wu et al., 2019). There is no significant evolution of the interatomic distances for the different shells between layered precursors and reflux products.

3.5. Co local environment

Co K-edge EXAFS spectra of selected samples display similar frequencies but contrasting amplitudes over the k-range probed (Fig. 3a), amplitudes decreasing in the order vernadite (CoV) to hollandite (CoV-Ba-Re), and to nsutite (CoV-pH4-Re-2d). The FTs of these Co K-edge EXAFS spectra (Fig. 3b) display three maxima at ~1.5, ~2.5, and ~3.0 Å (R+ΔR) that correspond to Co-O first shell, and Co-Me ESL and CSL, respectively (Simanova and Peña, 2015; Wu et al., 2019). FTs of CoV and CoV-pH4-Re-2d are essentially alike, except for a stronger intensity at ~2.5 Å (R+ΔR) in the

former sample. The maximum at ~2.5 Å (R+ΔR) is weakest for CoV-Ba-Re whereas the intensity at ~3.0 Å (R+ΔR) is highest, thus indicating different numbers of ESL and CSL, consistent with the CN_C/CN_E ratios derived from the simulation of Co K-edge EXAFS spectra (Fig. S3 and Table S2). Low Co-Me CSLs indicate the minor presence of Co sorbed at vacancy sites (Co^V) in CoV, whereas most Co (~81%) are structurally incorporated species (Co^S), consistent with previous reports (Manceau et al., 1997; Kwon et al., 2013; Simanova and Pena, 2015; Wu et al., 2019).

3.6. Nitric acid treatment

Consistent with previous reports (Wu et al., 2019, 2020), XRD patterns of CoV, CoV-pH4-Re-2d, and CoV-Ba collected after the nitric acid treatment display minor evolutions relative to the original ones (Fig. 4a), indicative of the limited modification of Mn oxide structure. Weak peaks at 4.9, 3.5, 3.1, 2.2, 1.8, and 1.55 Å, consistent with those of hollandite (ICDD #38-0476), are observed in CoV XRD pattern, however, thus confirming the formation of tunnel structures during the acid-wash treatment. Hollandite reflections are also detected in CoV-Ba XRD pattern after the acid treatment, although weaker than in CoV pattern. Reflection positions and intensities are essentially unchanged in CoV-Ba-Re pattern after the nitric acid treatment. By contrast, although the overall XRD profile of CoV-pH4-Re-2d appears unaffected by the acid treatment, reflections are systematically shifted towards smaller distances by this treatment. This minor contraction of the unit cell is consistent with the transformation from manganoan nsutite to ideal nsutite and is most likely related to the release to solution of Mn(II,III) from the solid (Zwicker et al., 1962).

Nitric acid treatment is an effective method to distinguish metal species in Mn oxides, as nitric acid is able to extract exchangeable and adsorbed metal cations without damaging significantly (limited reduction essentially) the manganese oxide framework (Wu et al., 2019). In the present work, Mn (Fig. 4b) and Co (Fig. 4c) releases do not reach a maximum after one week of acid treatment, although release rates are much

reduced compared to the initial rate. Mn is preferentially released from layered precursors compared to their reflux products, suggesting lower contents of soluble Mn(II,III) in the latter, consistent with results of the Combo method. Mn release, and Mn release rate after 24 hrs, is maximum for CoV.

During the acid-wash treatment, CoV-pH4-Re-2d releases ~49% of its Co content to solution, more than its layered precursor (~37%), and far more than CoV-Ba-Ex (~31%) and CoV-Ba-Ex-Re (~20%). The initial fast release of Co, that can be quantified from the intersect on the *y*-axis of the linear fitting to Co release during the final stages (>=24 hrs) of treatment, will be hereafter considered as sorbed Co (Co^V), whereas the remaining Co will be considered as structurally incorporated Co (Co^S). Accordingly, Co releases as a function of time indicate that Co^V and Co^S account for ~20 and ~80%, respectively, in layered precursors (Table 3), consistent with the results derived from fitting the Co K-edge EXAFS data and with previous reports of Co-speciation in birnessite and vernadite (Kwon et al., 2013; Simanova and Peña, 2015; Yin et al., 2015; Wu et al., 2019). On the other hand, Co^V and Co^S account for ~60 and ~40% of the Co species in CoV-pH4-Re-2d, although its overall Co-content is similar to that of layered precursors (Table 1). The contrasting distributions of Co species observed in CoV and CoV-pH4-Re-2d indicate that Co speciation is significantly altered along the mineralogical transformation from vernadite to manganoan nsutite. Specifically, part of Co (~20%) is likely released from vernadite layers and sorbed to reaction product. On the contrary, the similarity of CoV and CoV-Ba-Re Co K-edge EXAFS spectra suggests that relative proportions of Co^V and Co^S were not modified significantly during conversion of Ba-exchanged vernadite (CoV-Ba) to hollandite (CoV-Ba-Re – Table 3), consistent with previous report on todorokite formation from Co-containing layered precursors (Wu et al., 2019). The contrasting contents of Co^V and Co^S in CoV-Ba-Re and CoV-pH4-Re-2d are not correlated to their respective contents of CSL and ESL (Table S2). The high Co release ratio of CoV-pH4-Re-2d associated to its low CN_C/CN_E ratio possibly results from a high content of double-

corner sharing species.

Ba initially present as a hydrated exchangeable Ba^{2+} in CoV-Ba interlayers is readily released during the acid treatment (Fig. 4d). On the other hand, only ~8% of Ba is released from CoV-Ba-Re after a similar treatment, consistent with the coordination of Ba with O atoms forming hollandite 2×2 tunnels (Post et al., 1982; Miura, 1986). This behavior is specific to large Ba^{2+} cations (1.35 Å ionic radius in sixfold coordination – Shannon, 1976) when present in 2×2 tunnels as smaller cations, such as Cd^{2+} (0.78 Å ionic radius in sixfold coordination), could be present in tunnel sites as hydrated cations (Randall et al., 1998).

4. DISCUSSION

4.1. Formation of tectomanganates with different tunnel sizes from vernadite precursors

In the present work, both nsutite (intergrowth of 1×1 and 1×2 tunnels) and hollandite (2×2 tunnel size) were obtained from the reflux of Co-containing vernadite. The formation of tectomanganates with tunnel sizes lower than 2×2 complements previous reports of both hollandite/cryptomelane and todorokite (3×3 tunnel size) formation from layered precursors and supports the hypothesis of the major role of vernadite as a precursor in the formation of natural tectomanganates (Burns and Burns, 1978; Bodeï et al., 2007).

Environmental pH appears to strongly affect the nature of tectomanganates formed through its influence on tunnel dimension, as shown by the formation of pyrolusite, romanechite, and OMS-5 (1×1, 2×3, and 2×4 tunnel sizes, respectively) from the same layered precursor by varying pH conditions from 1, to 7, and to 13, respectively (Shen et al., 2005). Consistently, todorokite is obtained experimentally under neutral and weakly alkali or acidic conditions (pH 4.8-9 – Cui et al., 2005; Atkins et al., 2014), and formation of a tectomanganate with 4×4 tunnel size was reported at pH 6-8 from a

layered vernadite precursor in the presence of Mn(II) (Yang et al., 2018). To the authors' knowledge, there is no evidence of todorokite formation under low pH conditions (pH < 4.8), and Grangeon and coworkers showed that hollandite/cryptomelane formation was favored by the initial equilibration of the layered precursors at low pH (Grangeon et al., 2014, 2015), consistent with previous reports (Tu et al., 1994; Zhang et al., 2011). In the present work, hollandite was also formed at room temperature during the acid treatment (1 M H^+) of the vernadite precursor as well as under neutral condition during the reflux process (initial and final pH values: 7.50 and 6.12, respectively). In this case, Ba^{2+} or K^+ template the formation of 2×2 tunnels of hollandite and cryptomelane, respectively, owing to their appropriate radii (Post et al., 1982; Miura, 1986).

The influence of pH on tectomanganate tunnel size may be understood from the mechanisms driving the phyllomanganate-to-tectomanganate reaction. The presence of Mn(III) in phyllomanganate octahedral layers induces indeed steric strains owing to the Jahn-Teller distortion of $Mn(III)O_6$ octahedra (Drits et al., 1997; Gaillot et al., 2007). Mn(III) octahedra thus represent weak structural points, especially when aligned to minimize steric strains (Gaillot et al., 2007). Independent of the actual mechanism leading to the formation of tunnel walls (layer kinking or Mn(III) migration to the interlayer – Atkins et al., 2014, 2016; Grangeon et al., 2014, 2015), an increased proportion of Mn(III) favors the transformation process. Lowering the equilibration pH of the layered precursor thus appears to have a positive effect on the formation of tectomanganate with small tunnel sizes owing to the induced increase of Mn(III) in vernadite layers (Grangeon et al., 2014) and to the subsequent enhancement of Mn(III) disproportionation reaction (Manceau et al., 1997; Lanson et al., 2000). In the present case, disproportionation appears as an important step of the transformation as shown by the decreased content of Mn(III) in reflux products compared to Mn(IV) (Table 2). Enhancement of Mn(III) disproportionation and migration of Mn(II,III) from the layer to solution at low pH is supported by the presence of ideal and manganoan nsutite in CoV-0.5M H^+-Re and CoV-pH4-Re-2d, respectively. Mn(II,III) relative proportion is

indeed significantly lower in ideal nsutite than in manganoan nsutite (Zwicker et al., 1962), and in hollandite and todorokite (Wu et al., 2019). Similarly, the nitric acid treatment of CoV-pH4-Re-2d releases Mn(II,III) to solution and induces the conversion of manganoan nsutite to its ideal form (Fig. 4a).

Temperature may also influence the tunnel size in formed tectomanganates. Hollandite is formed indeed during CoV acid treatment (1 M H^+) at ambient temperature, whereas manganoan nsutite is formed during the reflux treatment of CoV-pH4 at 100 °C. Consistent with this hypothesis, formation of cryptomelane was reported after aging at room temperature of vernadite equilibrated at pH 3 (Grangeon et al., 2014). The enhanced formation of tectomanganates with increasing temperature is possibly related to the increased rate of Mn(III) disproportionation (Hanf et al., 2020) and release of Mn(II,III) to solution. Low-temperature formation of tectomanganates is likely common in natural environments, however, especially in anoxic and suboxic conditions owing to the presence of Mn(II,III) species (Yang et al., 2018).

4.2. Influence of Co on tectomanaganate formation, fate of Co during this process, and Co speciation in newly formed tectomanganates

It is commonly accepted that Co is mainly (~80%-100%) present as incorporated species in layered Mn oxides (Manceau et al., 1997; Kwon et al., 2013; Yin et al., 2014, 2015; Simanova and Peñna, 2015; Wu et al., 2019). Co(III) usually replaces Mn(III) isomorphously and its presence thus decreases the steric strains induced by the presence of these Jahn-Teller distorted octahedra in the layer (Manceau et al., 1997; Gaillot et al., 2007; Li et al., 2014; Yin et al., 2015) and impairs in turn the phyllomanganate-to-tectomanganate transformation (Wu et al., 2019). Accordingly, Co contents higher than ~5 at.% in birnessite precursors were recently shown to hamper their transformation to todorokite and to lead to increasingly disordered 3×n (3<n) products (Wu et al., 2019). For Me/(Me+Mn) ratios higher than 20 at.% (Me = Co, Ni), Co forms, often in association with Ni, an octahedral sheet sandwiched in between MnO_2 layers leading

to the minerals asbolane or lithiophorite, depending on the Al content (Chukrov et al., 1987; Manceau et al., 1987; Llorca and Monchoux, 1991; Roqué-Rosell et al., 2010; Lambiv Dzemua et al., 2013; Ploquin et al., 2019). The presence of this octahedral sheet has also been shown to impede the transformation of layered Mn oxides to tectomanganates (Wu et al., 2020).

For Co contents in layered precursors similar to those in the present study [~0.05 Co/(Co+Mn) molar ratios], tunnel structures are systematically formed, however, and the overall Co content of the precursors is maintained in the reflux products, whatever their nature (Wu et al., 2019). Evolution of Co local environment differs however depending on the mineralogy of the reflux product (todorokite, hollandite, nsutite). In todorokite, Co exhibits essentially ESL, being mostly located in Mn1/Mn3 sites (Wu et al., 2019). In hollandite, the proportion of structural Co is similar to that of its layered precursor (CoV-Ba and CoV-Ba-Re in Table 3), although the CN_C/CN_E ratio is significantly increased in the reflux product (from 0.36 in CoV to 0.96 in CoV-Ba-Re – Table S2). Although to a lower extent, this ratio is increased also in nsutite (0.50 in CoV-pH4-Re-2d – Table S2), that also contains ~20% more Co sorbed to the solid phase, as shown by the nitric acid treatment (~20 and ~40% Co^V in CoV and CoV-pH4-Re-2d, respectively – Table 3).

The contrasting behavior of Co in the reflux products most likely results from their structure, and more especially from the relative proportions of ESL and CSL. Tectomanganates with different tunnel sizes display indeed contrasting CN_C/CN_E ratios. In ideal todorokite, Mn2/Mn4 sites display 4 CSL and 4 ESL (Fig. S5), whereas Mn1/Mn3 sites only have 6 ESL, the ratio between the two sets of sites being constant at 2 (McKeown and Post, 2001). In hollandite, there is only one type of sites, similar to todorokite Mn2/Mn4 sites and thus displaying 4 CSL and 4 ESL. Although less favorable than sites displaying mostly ESL, these sites are also suitable to host structural Co. Finally, nsutite possesses two types of octahedral sites, one similar to the Mn2/Mn4 sites of todorokite (4 CSL and 4 ESL) whereas the other site displays 8 CSL

and 2 ESL (Fig. S5), as in pyrolusite (McKeown and Post, 2001). Depending on the relative proportions of pyrolusite and of ramsdellite fragments in nsutite, the ratio of these two sites varies significantly.

As tunnel size decreases from todorokite to nsutite, the CN_C/CN_E ratio thus increases significantly. The predominant occurrence of Co in Mn1/Mn3 sites of todorokite (Wu et al., 2019) is consistent with the increased stability of Co^S compared to Co^V in phyllomanganates shown by DFT calculations (Kwon et al., 2013). Although less favorable than sites displaying mostly ESL, hollandite Mn sites and possibly equivalent todorokite Mn2/Mn4 sites, are also suitable to host structural Co, as shown by the similar proportion of structural Co in CoV-Ba and CoV-Ba-Re (Table 3). On the contrary, octahedral sites in nsutite pyrolusite-like fragments are most likely not appropriate to accommodate Co, owing to their higher CN_C/CN_E ratio. As a result, ~20% of Co initially present in CoV-pH4 migrate out of the solid during the transformation process, before being sorbed on the newly formed tectomanganate. Natural Co contents in tectomanganates having small tunnel sizes are thus lower than those found in tectomanganates with medium-to-large small tunnel sizes (e.g., Taylor et al., 1964; Lambiv Dzemua et al. 2013).

As a consequence, Co is preferentially enriched in natural phyllomanganates compared to tectomanganates (Taylor et al., 1964; Taylor and Mckenzie, 1966; Taylor, 1968; Burns and Burns, 1977; Chukhrov and Gorshkov, 1980; Chukhrov et al., 1980; Chukhrov, 1982; Ostwald, 1984; Llorca, 1987; Manceau et al., 1987, 1992; Burlet and Vanbrabant, 2015). When possible, the subsequent transformation of Co-rich phyllomanganates will lead to structures exhibiting large tunnel sizes, such as a-disordered todorokite, in which Co can remain structurally incorporated. Transformation operating at lower pH values will result in formation of tunnel structures having smaller tunnel sizes, however. In this case, part of the Co initially present in the phyllomanganate will be released from the octahedral layers and/or sorbed at the surface of newly formed tectomanganates, thus potentially favoring

subsequent release of Co to solution.

5. CONCLUSION

Depending on environmental conditions, phyllomanganate transformation may lead to tectomanganates exhibiting a variety of tunnel sizes (Fig. 5), even at low temperature, and the present study provides significant new insights into the geochemical conditions controlling tunnel size of formed tectomanganates. Large tunnel sizes are favored under circum-neutral conditions (pH 4.8-9), the actual tunnel size being in this case influenced by the nature of interlayer cation in the layered precursor (Mg: todorokite, K/Ba: cryptomelane/hollandite). Under acidic conditions (pH < 4.8), both the increase of Mn(III) content in the layers of phyllomanganate precursors, and the subsequent enhancement of Mn(III) disproportionation during their transformation contribute to the formation of tectomanganates with small tunnel sizes.

In turn, the fate of Co structurally incorporated in layered precursors is also influenced by the pH conditions of the transformation. For Co contents lower than 5-10 at.%, the transformation to tectomanganates is essentially unaffected and most Co remains structurally incorporated in the newly formed tectomanganates formed under circum-neutral conditions (todorokite, hollandite, cryptomelane). Under acidic conditions, part of Co present in layered precursors is released to solution and/or sorbed at the surface of the tectomanganates having small tunnel sizes (nsutite, pyrolusite) owing to the reduced stability of Co(III) octahedra when the relative proportion of corner-sharing linkages increases. As Co(III) replaces Mn(III) isomorphously, its presence decreases the steric strains induced by the presence within the octahedral layer of these Jahn-Teller distorted octahedra and impairs the phyllomanganate-to-tectomanganate transformation when its content exceeds 5-10 at.% (Wu et al., 2019). The present results thus account for the natural prevalence of Co in phyllomanganates compared to tectomanganates, and in tectomanganates having large tunnel sizes compared to small ones, in which Co occurs as sorbed species to a large extent. By

unraveling Co affinity for different Mn oxides, the present study thus contributes to a better understanding of the cycling of Co, and more generally of transition metals associated to environmentally relevant Mn oxides.

Declaration of competing interest

The authors declare that they have no known competing financial interests or personal relationships that could have appeared to influence the work reported in this paper.

ACKNOWLEDGEMENTS

The authors are grateful to Dr. Lirong Zheng at BSRF for his assistance with XAS data collection and analysis. The assistance of Martine Lanson and Nathaniel Findling (Geochemistry & Mineralogy platform, ISTerre, Grenoble) for elemental analyses and XRD data collection, respectively, is gratefully acknowledged. This work is supported by the National Key Research and Development Program of China (No. 2016YFD0800400) and the Natural Science Foundations of China (No. 41571448). Xionghan Feng, Bruno Lanson, and Zhongkuan Wu are supported by a Cai Yuanpei program between the Key Laboratory of Arable Land Conservation (Wuhan, China) and ISTerre (Grenoble, France). ISTerre is part of Labex OSUG@2020 (ANR10 LABX56).

RESEARCH DATA

Research Data associated with this article can be accessed at https://doi.org/10.17632/27369v78sv.2

REFERENCES

Asavin A.M., Daryin A.V. and Melnikov M.E. (2015) Microrhythmic distribution of Co, Mn, Ni, and La contents in cobalt-rich ferromanganese crusts from the Magellan seamounts. *Geochem. Int.* **53**, 19-38.

Atkins A.L., Shaw S. and Peacock C.L. (2014) Nucleation and growth of todorokite from birnessite: Implications for trace-metal cycling in marine sediments. *Geochim. Cosmochim. Acta* **144**, 109-125.

Atkins A.L., Shaw S. and Peacock C.L. (2016) Release of Ni from birnessite during transformation of birnessite to todorokite: Implications for Ni cycling in marine sediments. *Geochim. Cosmochim. Acta* **189**, 158-183.

Bargar J.R., Tebo B.M., Bergmann U., Webb S.M., Glatzel P., Chiu V.Q. and Villalobos M. (2005) Biotic and abiotic products of Mn(II) oxidation by spores of the marine *Bacillus* sp.strain SG-1. *Amer. Mineral.* **90**, 143-154.

Bodeï S., Manceau A., Geoffroy N., Baronnet A. and Buatier M. (2007) Formation of todorokite from vernadite in Ni-rich hemipelagic sediments. *Geochim. Cosmochim. Acta* **71**, 5698-5716.

Bonatti E., Kraemer T. and Rydell H., 1972. Classification and genesis of submarine iron-manganese deposits, in: Horn, D. (Ed.), Ferromanganese deposits on the ocean floor. National Science Foundation, Washington, D.C., pp. 149-166.

Burlet C. and Vanbrabant Y. (2015) Study of the spectro-chemical signatures of cobalt-manganese layered oxides (asbolane-lithiophorite and their intermediates) by Raman spectroscopy. *J. Raman Spectr.* **46**, 941-952.

Burns R.G. and Burns V.M. (1977) The mineralogy and crystal chemistry of deep-sea manganese nodules, a polymetallic resource of the twenty-first century. *Phil. Trans. Roy. Soc. London A* **286**, 283-301.

Burns V.M. and Burns R.G. (1978) Post-depositional metal enrichment processes inside manganese nodules from north equatorial pacific. *Earth Planet. Sci. Lett.* **39**, 341-348.

569 Choi J.H. and Hariya Y. (1992) Geochemistry and depositional environment of Mn
570 oxide deposits in the Tokoro Belt, northeastern Hokkaido, Japan. *Econ. Geol.* **87**,
571 1265-1274.
572 Chukhrov F.V. (1982) Crystallochemical nature of Co-Ni asbolan. *Int. Geol. Rev.* **24**,
573 598-604.
574 Chukhrov F.V., Drits V.A., and Gorshkov A.I. (1987) Structural transformations of
575 Manganese oxides in oceanic nodules. *International Geology Review* **29**, 110-
576 121.
577 Chukhrov F.V. and Gorshkov A.I. (1980) Reply to R. Giovanoli's comment. *Miner.*
578 *Depos.* **15**, 255-257.
579 Chukhrov F.V., Gorshkov A.I., Rudnitskaya E.S., Beresovskaya V.V. and Sivtsov A.V.
580 (1980) Manganese minerals in clays; a review. *Clays Clay Miner.* **28**, 346-354.
581 Chukhrov F.V., Gorshkov A.I. and Sivtsov A.V. (1981) A new todorokite structural
582 variety. *Izvestiya Akademii Nauk SSSR Seriya Geologicheskaya* **5**, 88-91.
583 Cui H.J., Feng X.H., Liu F., Tan W.F. and He J.Z. (2005) Factors governing formation
584 of todorokite at atmospheric pressure. *Sci. China Ser. D* **48**, 1678-1689.
585 Dekoninck A., Monié P., Blockmans S., Hatert F., Rochez G. and Yans J. (2019)
586 Genesis and 40Ar/39Ar dating of K-Mn oxides from the Stavelot Massif
587 (Ardenne, Belgium): Insights into Oligocene to Pliocene weathering periods in
588 Western Europe. *Ore Geol. Rev.* **115**, 103191.
589 Drits V.A., Lanson B. and Gaillot A.C. (2007) Birnessite polytype systematics and
590 identification by powder X-ray diffraction. *Amer. Mineral.* **92**, 771-788.
591 Drits V.A., Silvester E., Gorshkov A.I. and Manceau A. (1997) Structure of synthetic
592 monoclinic Na-rich birnessite and hexagonal birnessite: I. Results from X-ray
593 diffraction and selected-area electron diffraction. *Amer. Mineral.* **82**, 946-961.
594 Feng X.H., Tan W.F., Liu F., Wang J.B. and Ruan H.D. (2004) Synthesis of todorokite
595 at atmospheric pressure. *Chem. Mater.* **16**, 4330-4336.
596 Gaillot A.-C., Drits V.A., Manceau A. and Lanson B. (2007) Structure of the synthetic

K-rich phyllomanganate birnessite obtained by high-temperature decomposition of $KMnO_4$. *Micropor. Mesopor. Mater.* **98**, 267-282.

Golden D.C., Chen C.C. and Dixon J.B. (1986) Synthesis of todorokite. *Science* **231**, 717-719.

Golden D.C., Chen C.C. and Dixon J.B. (1987) Transformation of birnessite to buserite, todorokite, and manganite under mild hydrothermal treatment. *Clays Clay Miner.* **35**, 271-280.

Grangeon S., Fernandez-Martinez A., Warmont F., Gloter A., Marty N., Poulain A. and Lanson B. (2015) Cryptomelane formation from nanocrystalline vernadite precursor: a high energy X-ray scattering and transmission electron microscopy perspective on reaction mechanisms. *Geochem. Trans.* **16**, 12.

Grangeon S., Lanson B. and Lanson M. (2014) Solid-state transformation of nanocrystalline phyllomanganate into tectomanganate: influence of initial layer and interlayer structure. *Acta Crystallogr. B* **70**, 828-838.

Grangeon S., Lanson B., Lanson M. and Manceau A. (2008) Crystal structure of Ni-sorbed synthetic vernadite: a powder X-ray diffraction study. *Mineral. Mag.* **72**, 1279-1291.

Grangeon S., Lanson B., Miyata N., Tani Y. and Manceau A. (2010) Structure of nanocrystalline phyllomanganates produced by freshwater fungi. *Amer. Mineral.* **95**, 1608-1616.

Hanf L., Henschel J., Diehl M., Winter M. and Nowak S. (2020) Mn^{2+} or Mn^{3+}? Investigating transition metal dissolution of manganese species in lithium ion battery electrolytes by capillary electrophoresis. *Electrophoresis* **41**, 697-704.

Hein J.R., Schwab W.C. and Davis A.S. (1988) Cobalt-rich and platinum-rich ferromanganese crusts and associated substrate rocks from the Marshall-Islands. *Mar. Geol.* **78**, 255-283.

Kay J.T., Conklin M.H., Fuller C.C. and O'Day P.A. (2001) Processes of nickel and cobalt uptake by a manganese oxide forming sediment in Pinal Creek, Globe

625 Mining District, Arizona. *Environ. Sci. Technol.* **35**, 4719-4725.
626 Kim H.S., Pasten P.A., Gaillard J.F. and Stair P.C. (2003) Nanocrystalline todorokite-
627 like manganese oxide produced by bacterial catalysis. *J. Am. Chem. Soc.* **125**,
628 14284-14285.
629 Kwon K.D., Refson K. and Sposito G. (2013) Understanding the trends in transition
630 metal sorption by vacancy sites in birnessite. *Geochim. Cosmochim. Acta* **101**,
631 222-232.
632 Lambiv Dzemua G., Gleeson S.A. and Schofield P.F. (2013) Mineralogical
633 characterization of the Nkamouna Co–Mn laterite ore, southeast Cameroon.
634 *Miner. Depos.* **48**, 155-171.
635 Lanson B., Drits V.A., Feng Q. and Manceau A. (2002) Structure of synthetic Na-
636 birnessite: Evidence for a triclinic one-layer unit cell. *Amer. Mineral.* **87**, 1662-
637 1671.
638 Lanson B., Drits V.A., Silvester E. and Manceau A. (2000) Structure of H-exchanged
639 hexagonal birnessite and its mechanism of formation from Na-rich monoclinic
640 buserite at low pH. *Amer. Mineral.* **85**, 826-838.
641 Lanson B., Marcus M.A., Fakra S., Panfili F., Geoffroy N. and Manceau A. (2008)
642 Formation of Zn–Ca phyllomanganate nanoparticles in grass roots. *Geochim.*
643 *Cosmochim. Acta* **72**, 2478-2490.
644 Li H., Liu F., Zhu M.Q., Feng X.H., Zhang J. and Yin H. (2015) Structure and
645 properties of Co-doped cryptomelane and its enhanced removal of Pb^{2+} and Cr^{3+}
646 from wastewater. *J Environ. Sci. (China)* **34**, 77-85.
647 Li X., Ma X., Su D., Liu L., Chisnell R., Ong S.P., Chen H., Toumar A., Idrobo J.-C.,
648 Lei Y., Bai J., Wang F., Lynn J.W., Lee Y.S. and Ceder G. (2014) Direct
649 visualization of the Jahn–Teller effect coupled to Na ordering in $Na_{5/8}MnO_2$. *Nat.*
650 *Mater.* **13**, 586-592.
651 Llorca S. (1987) Nouvelles données sur la composition et la structure des
652 lithiophorites d'après de échantillons de Nouvelle-Calédonie. *C. R. Acad. Sci.*

653 *Paris - Série II* **304**, 15-18.
654 Llorca S. and Monchoux P. (1991) Supergene cobalt minerals from New Caledonia.
655 *Can. Mineralog.* **29**, 149-161.
656 Luo Y., Tan W.F., Suib S.L., Qiu G.H. and Liu F. (2018) Dissolution and phase
657 transformation processes of hausmannite in acidic aqueous systems under anoxic
658 conditions. *Chem. Geol.* **487**, 54-62.
659 Manceau A., Gorshkov A.I. and Drits V.A. (1992) Structural chemistry of Mn, Co,
660 and Ni in manganese hydrous oxides. I. Information from EXAFS spectroscopy
661 and electron and X-ray diffraction. *Amer. Mineral.* **77**, 1144-1157.
662 Manceau A., Lanson M. and Geoffroy N. (2007) Natural speciation of Ni, Zn, Ba, and
663 As in ferromanganese coatings on quartz using X-ray fluorescence, absorption,
664 and diffraction. *Geochim. Cosmochim. Acta* **71**, 95-128.
665 Manceau A., Llorca S. and Calas G. (1987) Crystal chemistry of cobalt and nickel in
666 lithiophorite and asbolane from New Caledonia. *Geochim. Cosmochim. Acta* **51**,
667 105-113.
668 Manceau A., Marcus M.A. and Grangeon S. (2012) Determination of Mn valence
669 states in mixed-valent manganates by XANES spectroscopy. *Amer. Mineral.* **97**,
670 816-827.
671 Manceau A., Silvester E., Bartoli C., Lanson B. and Drits V.A. (1997) Structural
672 mechanism of Co^{2+} oxidation by the phyllomanganate buserite. *Amer. Mineral.*
673 **82**, 1150-1175.
674 Marcus M.A., Manceau A. and Kersten M. (2004) Mn, Fe, Zn and As speciation in a
675 fast-growing ferromanganese marine nodule. *Geochim. Cosmochim. Acta* **68**,
676 3125-3136.
677 McKenzie R.M., 1989. Manganese Oxides and Hydroxides, in: Dixon, J.B., Weed,
678 S.B. (Eds.), Minerals in Soil Environments. Soil Science Society of America,
679 Madison, Wisconsin, USA, pp. 439-465.
680 McKeown D.A. and Post J.E. (2001) Characterization of manganese oxide

mineralogy in rock varnish and dendrites using X-ray absorption spectroscopy. *Amer. Mineral.* **86**, 701-713.

Miura H. (1986) The crystal structure of hollandite. *Mineral. J.* **13**, 119-129.

Mücke A., Dzigbodi-Adjimah K. and Annor A. (1999) Mineralogy, petrography, geochemistry and genesis of the Paleoproterozoic Birimian manganese-formation of Nsuta/Ghana. *Miner. Depos.* **34**, 297-311.

Nicholson K. (1992) Contrasting mineralogical-geochemical signatures of manganese oxides; guides to metallogenesis. *Econ. Geol.* **87**, 1253-1264.

Ostwald J. (1984) Some observations on the 7 Å X-ray reflection in marine manganese nodules. *Neues Jahrb. Mineral. - Mh.*, 1-8.

Parc S., Nahon D., Tardy Y. and Vieillard P. (1989) Estimated solubility products and fields of stability for cryptomelane, nsutite, birnessite, and lithiophorite based on natural lateritic weathering sequences. *Amer. Mineral.* **74**, 466-475.

Peacock C.L. and Sherman D.M. (2007) Crystal-chemistry of Ni in marine ferromanganese crusts and nodules. *Amer. Mineral.* **92**, 1087-1092.

Ploquin F., Fritsch E., Guigner J.M., Esteve I., Delbes L., Dublet G. and Juillot F. (2019) Phyllomanganate vein-infillings in faulted and Al-poor regoliths of the New Caledonian ophiolite: periodic and sequential crystallization of Ni–asbolane, Alk–birnessite and H–birnessite. *Eur. J. Mineral.* **31**, 335-352.

Post J.E. (1999) Manganese oxide minerals: Crystal structures and economic and environmental significance. *Proc. Nat. Acad. Sci.* **96**, 3447-3454

Post J.E., Vondreele R.B. and Buseck P.R. (1982) Symmetry and cation displacements in hollandites - structure refinements of hollandite, cryptomelane and priderite. *Acta Crystallogr. Sect. B-Struct. Commun.* **38**, 1056-1065.

Randall S.R., Sherman D.M. and Ragnarsdottir K.V. (1998) An extended X-ray absorption fine structure spectroscopy investigation of cadmium sorption on cryptomelane (KMn_8O_{16}). *Chem. Geol.* **151**, 95-106.

Ravel B. and Newville M. (2005) ATHENA and ARTEMIS: interactive graphical data

709 analysis using IFEFFIT. *Phys. Scripta* **2005**, 1007.
710 Roqué-Rosell J., Mosselmans J.F.W., Proenza J.A., Labrador M., Galí S., Atkinson
711 K.D. and Quinn P.D. (2010) Sorption of Ni by "lithiophorite–asbolane"
712 intermediates in Moa Bay lateritic deposits, eastern Cuba. *Chem. Geol.* **275**, 9-18.
713 Said M.I. (2020) Akhtenskite-nsutite phases: Polymorphic transformation, thermal
714 behavior and magnetic properties. *J. Alloys Compounds* **819**, 152976.
715 Shannon R.D. (1976) Revised effective ionic radii and systematic studies of
716 interatomic distances in halides and chalcogenides. *Acta Crystallogr. A* **32**, 751-
717 767.
718 Shen X.F., Ding Y.S., Liu J., Cai J., Laubernds K., Zerger R.P., Vasiliev A., Aindow
719 M. and Suib S.L. (2005) Control of nanometer-scale tunnel sizes of porous
720 manganese oxide octahedral molecular sieve nanomaterials. *Adv. Mater.* **17**, 805-
721 809,785.
722 Simanova A.A. and Peña J. (2015) Time-Resolved Investigation of Cobalt Oxidation
723 by Mn(III)-Rich delta-MnO_2 Using Quick X-ray Absorption Spectroscopy.
724 *Environ. Sci. Technol.* **49**, 10867-10876.
725 Taylor R. (1968) The association of manganese and cobalt in soils—further
726 observations. *J. Soil Sci.* **19**, 77-80.
727 Taylor R. and Mckenzie R. (1966) The association of trace elements with manganese
728 minerals in Australian soils. *Aust. J. Soil Res.* **4**, 29.
729 Taylor R.M., Mckenzie R.M. and Norrish K. (1964) The mineralogy and chemistry of
730 manganese in some Australian soils. *Soil Res.* **2**, 235-248.
731 Toner B., Manceau A., Webb S.M. and Sposito G. (2006) Zinc sorption to biogenic
732 hexagonal-birnessite particles within a hydrated bacterial biofilm. *Geochim.*
733 *Cosmochim. Acta* **70**, 27-43.
734 Tu S.H., Racz G.J. and Goh T.B. (1994) Transformations of synthetic birnessite as
735 affected by pH and manganese concentration. *Clays Clay Miner.* **42**, 321-330.
736 Turner S. and Buseck P.R. (1983) Defects in nsutite (gamma-mno2) and dry-cell

battery efficiency. *Nature* **304**, 143-146.

Villalobos M., Lanson B., Manceau A., Toner B. and Sposito G. (2006) Structural model for the biogenic Mn oxide produced by *Pseudomonas putida*. *Amer. Mineral.* **91**, 489-502.

Villalobos M., Toner B., Bargar J. and Sposito G. (2003) Characterization of the manganese oxide produced by *Pseudomonas putida* strain MnB1. *Geochim. Cosmochim. Acta* **67**, 2649-2662.

Vodyanitskii Y.N. (2006) The composition of Fe-Mn nodules as determined by synchrotron X-ray analysis (Review of publications). *Euras. Soil Sci.* **39**, 147-156.

Vodyanitskii Y.N. (2009) Mineralogy and geochemistry of manganese: A review of publications. *Euras. Soil Sci.* **42**, 1170-1178.

Webb S.M., Tebo B. and Bargar J. (2005) Structural characterization of biogenic Mn oxides produced in seawater by the marine *Bacillus* sp. strain SG-1. *Amer. Mineral.* **90**, 1342-1357.

Wegorzewski A.V., Grangeon S., Webb S.M., Heller C. and Kuhn T. (2020) Mineralogical transformations in polymetallic nodules and the change of Ni, Cu and Co crystal-chemistry upon burial in sediments. *Geochim. Cosmochim. Acta* **282**, 19-37.

Wu Z., Lanson B., Feng X., Yin H., Qin Z., Wang X., Tan W., Chen Z., Wen W. and Liu F. (2020) Transformation of Ni-containing birnessite to tectomanganate: Influence and fate of weakly bound Ni(II) species. *Geochim. Cosmochim. Acta* **271**, 96-115.

Wu Z., Peacock C.L., Lanson B., Yin H., Zheng L., Chen Z., Tan W., Qiu G., Liu F. and Feng X. (2019) Transformation of Co-containing birnessite to todorokite: Effect of Co on the transformation and implications for Co mobility. *Geochim. Cosmochim. Acta* **246**, 21-40.

Yang P., Lee S., Post J.E., Xu H.F., Wang Q., Xu W.Q. and Zhu M.Q. (2018) Trivalent

765 manganese on vacancies triggers rapid transformation of layered to tunneled
766 manganese oxides (TMOs): Implications for occurrence of TMOs in low-
767 temperature environment. *Geochim. Cosmochim. Acta* **240**, 173-190.
768 Yin H., Li H., Wang Y., Ginder-Vogel M., Qiu G., Feng X., Zheng L. and Liu F.
769 (2014) Effects of Co and Ni co-doping on the structure and reactivity of
770 hexagonal birnessite. *Chem. Geol.* **381**, 10-20.
771 Yin H., Liu Y., Koopal L.K., Feng X., Chu S., Zhu M. and Liu F. (2015) High Co-
772 doping promotes the transition of birnessite layer symmetry from orthogonal to
773 hexagonal. *Chem. Geol.* **410**, 12-20.
774 Yin H., Tan W., Zheng L., Cui H., Qiu G., Liu F. and Feng X. (2012) Characterization
775 of Ni-rich hexagonal birnessite and its geochemical effects on aqueous Pb^{2+}/Zn^{2+}
776 and As(III). *Geochim. Cosmochim. Acta* **93**, 47-62.
777 Zhang Q., Xiao Z.D., Feng X.H., Tan W.F., Qiu G.H. and Liu F. (2011) alpha-MnO2
778 nanowires transformed from precursor delta-MnO2 by refluxing under ambient
779 pressure: The key role of pH and growth mechanism. *Mater. Chem. Phys.* **125**,
780 678-685.
781 Zhao H.Y., Liang X.R., Yin H., Liu F., Tan W.F., Qiu G.H. and Feng X.H. (2015)
782 Formation of todorokite from "c-disordered" H^{+}-birnessites: the roles of average
783 manganese oxidation state and interlayer cations. *Geochem. Trans.* **16**, 11.
784 Zwicker W.K., Jaffe H.W. and Meijer W.O.J. (1962) Nsutite-a widespread manganese
785 oxide mineral. *Amer. Mineral.* **47**, 246-266.
786

TABLES

Table 1

Elemental composition of selected samples

Sample	Mn wt.%	Co wt.%	Co at.%	Ba at.%	K at.%	Na at.%
CoV	56.1(7)	3.24(8)	5.11	n.d.	4.7	1.4
CoV-pH4	55.7(4)	3.23(6)	5.12	n.d.	3.0	n.d.
CoV-pH4-Re-1h	60.9(4)	3.55(6)	5.16	n.d.	2.8	n.d.
CoV-pH4-Re-2d	65.1(2)	3.71(2)	5.05	n.d.	1.6	n.d.
CoV-Ba	48.4(9)	2.89(6)	5.28	8.5	n.d.	3.5
CoV-Ba-Re	56.3(0)	3.36(0)	5.28	7.9	n.d.	2.6

Note: at.% values are calculated as Me/(Co+Mn); n.d. stands for not detected.

Table 2

Relative proportions of Mn (II), (III), and (IV) valence states determined fitting Mn K-edge XANES spectra 1st derivative (Combo method – Manceau et al., 2012) and resulting Mn average oxidation state (AOS).

Sample	Mn(II) at.%	Mn(III) at.%	Mn(IV) at.%	Mn-AOS
CoV	9	30	60	3.51
CoV-pH4	10	26	65	3.55
CoV-pH4-Re-1h	6	22	72	3.66
CoV-pH4-Re-3h	5	25	70	3.65
CoV-pH4-Re-2d	2	23	75	3.72
CoV-0.5M H^+-Re-2d	1	8	91	3.90
CoV-Ba	6	24	70	3.63
CoV-Ba-Re	1	18	80	3.79

Table 3

Relative proportions of Co species in layered precursors and reflux products.

Samples	Co^S/Co at.%	Co^V/Co at.%	Co^S/(Mn+Co) at.%	Co^V/(Mn+Co) at.%
CoV	78	22	3.99	1.12
CoV-pH4-Re-2d	59	41	2.98	2.07
CoV-Ba	82	18	4.33	0.95
CoV-Ba-Re	84	16	4.44	0.84

*Note: The proportions of Co^V are determined from the intercept of the linear fit to the slow release portion of the elemental release curves during the nitric acid treatment (Fig. 4).

804 **FIGURES**

805

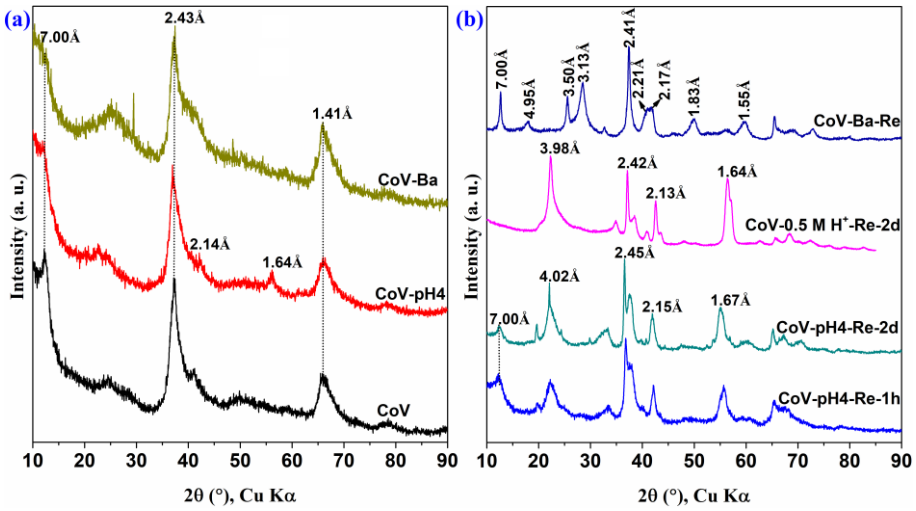

806

807 Fig. 1. XRD patterns of layered precursors (a) and of their reflux products (b)

808

809

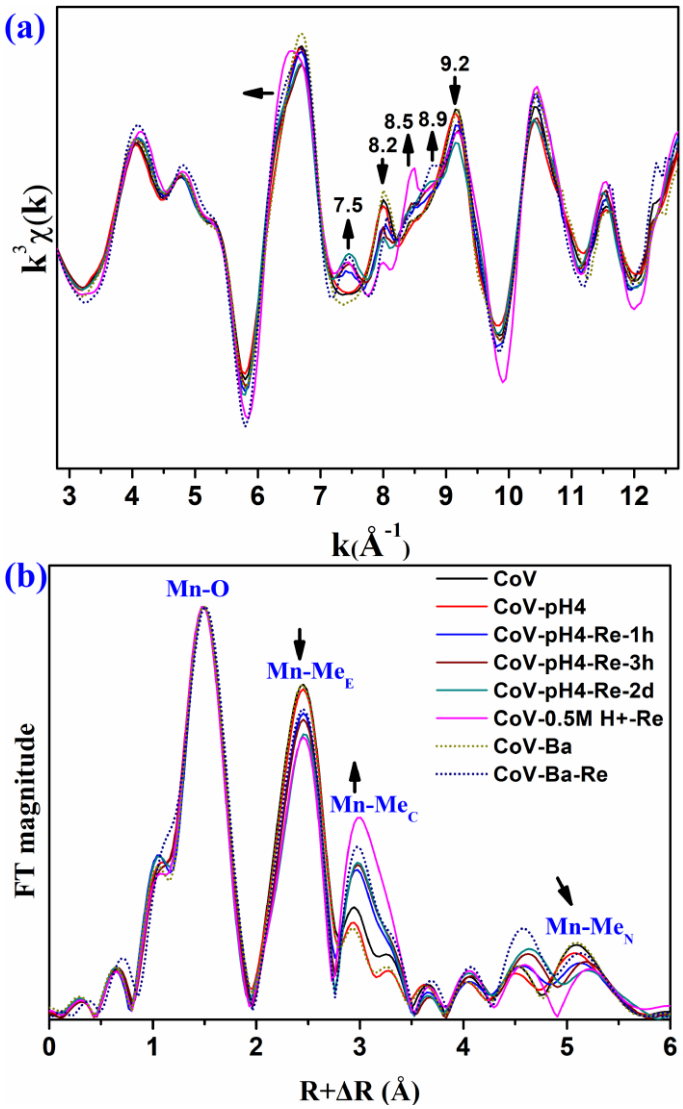

810

811 Fig. 2. Mn K-edge EXAFS spectra (a) and corresponding Fourier transforms (FT – b).

812 FT intensities are normalized to the ~1.5 Å (R+ΔR) maximum that corresponds to the

813 first Mn-O shell.

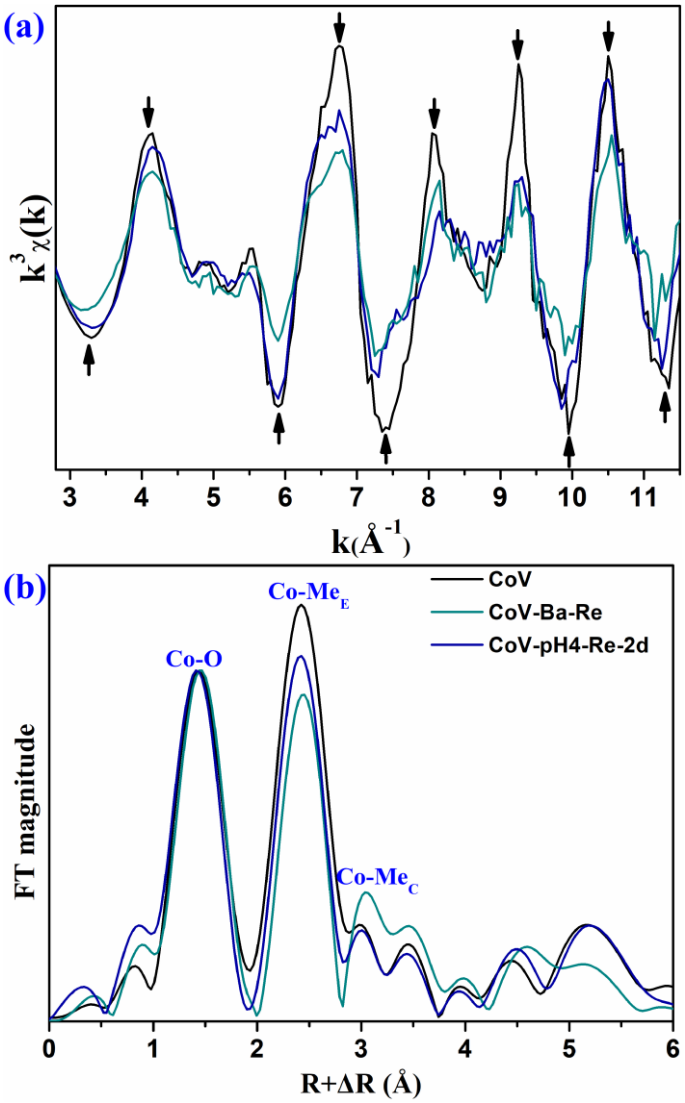

814

815 Fig. 3. Co K-edge EXAFS spectra (a) and corresponding Fourier transforms (FT – b).

816 Arrows in (a) highlight the amplitude decrease from CoV to CoV-Ba-Re and to CoV-

817 pH4-Re-2d. FT intensities are normalized to the ~1.5 Å (R+ΔR) maximum that

818 corresponds to the first Co-O shell.

819

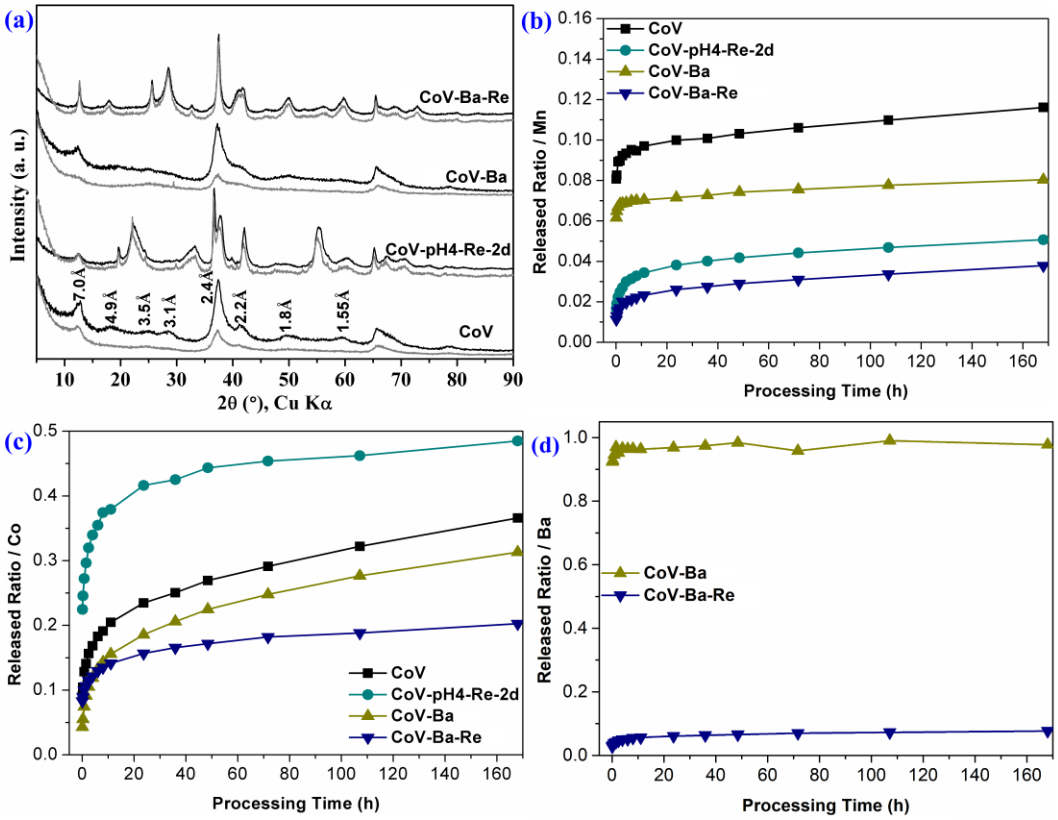

Fig. 4. Influence of the nitric acid-wash treatment on layered precursors and reflux products. XRD patterns before (gray) and after (black) the acid treatment (a). Elemental release from the solid during the treatment: Mn (b); Co (c); Ba (d). Co release curves are divided in two segments: data points before (not included) and after (included) 24 hrs define the fast and slow release stages, respectively. The slow release section is linearly fitted, the intercept of the equation approximating the amount of adsorbed species (CoV: $\%Co_{rel}$ = 0.0009x+0.2211, R^2 = 0.9845; CoV-pH4-Re-2d: $\%Co_{rel}$ = 0.0004x+0.4138, R^2 = 0.9254; CoV-Ba: $\%Co_{rel}$ =0.0009x+0.1775, R^2 = 0.9646; CoV-Ba-Re $\%Co_{rel}$ = 0.0003x+0.1552, R^2 = 0.9459)

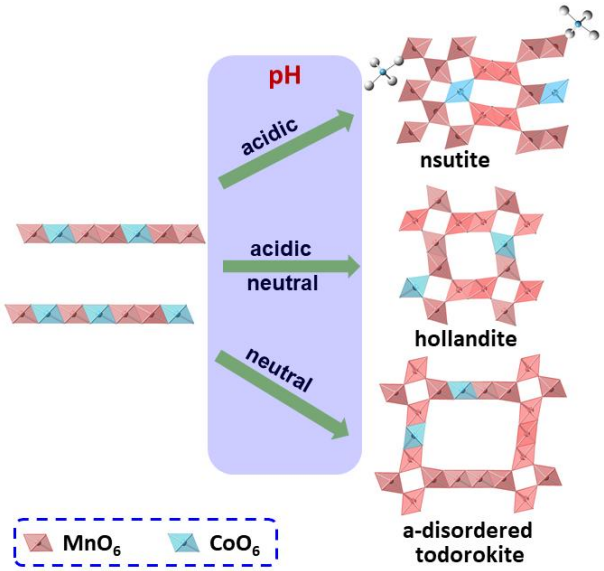

Fig. 5. Schematic of transformation for Co-containing vernadite to tectomanganates with various tunnel sizes and behaviours of Co